SPATIALLY RESOLVED STIS SPECTROSCOPY OF α ORIONIS: EVIDENCE FOR NON-RADIAL CHROMOSPHERIC OSCILLATION FROM DETAILED MODELING[1]

A. Lobel and A. K. Dupree
Harvard-Smithsonian Center for Astrophysics, 60 Garden Street, Cambridge MA 02138
(alobel@cfa.harvard.edu, adupree@cfa.harvard.edu)

ABSTRACT

Four spatially resolved near-UV raster scans across the chromospheric disk of α Ori, obtained with the Space Telescope Imaging Spectrograph on the *Hubble Space Telescope* reveal mean chromospheric infall from 1998 January to 1998 April, which reversed to upflow in deeper layers between 1998 September and 1999 March. In 1998 September we detect systematic reversals in the component maxima of four double-peaked emission lines of Si I (UV 1), Fe II (UV 36), Fe II (UV 61), and Al II] (UV 1), when scanning across the UV disk. Detailed modeling of the Si I $\lambda 2516$ resonance line with radiative transport calculations in spherical geometry constrain the mean radial velocity structure in the projected slit area (25 by 100 mas) for different aperture positions, observed off-limb to 157.5 mas. Hence we determine with semi-empirical models that these spatial reversals of emission line components correspond with average opposite flow velocities of ~ 2 km s^{-1} across the chromospheric disk. We determine that the chromospheric velocity field can not be represented by a unique radial velocity structure across the stellar disk in order to match the observed peak ratios of this raster scan. These sub-sonic velocities indicate (local) non-radial movements of chromospheric fluid in confined regions during a chromospheric oscillation phase, which reverses from global contraction into expansion over this monitoring period of 15 months.

Subject headings: stars: chromospheres — stars: individual (α Orionis) — stars: late-type — supergiants

1. INTRODUCTION

Spatially resolved spectroscopic observations of gas dynamics in the atmospheres of stars other than the Sun are physically limited for various reasons, although they represent one of the most challenging measurements to improve our comprehension of stellar environments. Doppler information from ground-based optical high-resolution spectroscopy of spatially resolvable targets is restricted by the quality of seeing conditions through Earth's atmosphere, typically to the level of one arcsecond in 'good weather' conditions. Kinematic and morphologic studies of high-velocity winds from hot supergiants indicate axis-symmetric nebulae (i.e. Pasquali, Nota, & Clampin 1999), although remnants from asymmetric mass ejection have also been observed (Meaburn, López, & O'Conner 1999). Spectroscopic mapping studies of the low-speed winds from cool supergiants are scarce due to a natural deficiency of sufficiently nearby targets with resolvable optically bright circumstellar environments. Mauron (1990) detected profile changes in the spatially resolved K I (fluorescent) resonance emission line of α Ori (M2 Iab, HD39801), obtained off-limb at 5$''$ and 7.5$''$ from a scattering gas (and dust) shell which extends to at least 50$''$ (Honeycutt et al. 1980) around this cool supergiant. Mauron & Querci (1990) also scanned the Na I D lines of α Ori and μ Cep (M2 Iae) at 6$''$, 10$''$, and 12$''$ above the limb. These emission profiles reveal variable substructures for different slit positions and orientations. For μ Cep they are interpreted to result from (incomplete) circumstellar

shells with different expansion velocities. Telluric Na I doublet emission at the short-wavelength side of these line profiles has been suggested to explain their double-peaked appearance in α Ori. We note that the detailed profiles of these optically thick lines bear however a striking resemblance to the self-absorbed line structure of many optically thick (fluorescent) emission lines of neutral and singly-ionized metals, observed with IUE and HST-GHRS (Goddard High Resolution Spectrograph) in the near-UV spectrum of α Ori (e.g. Brandt et al. 1995; Carpenter & Robinson 1997).

The advent of space-borne spectroscopy has recently enabled high-resolution measurements at the subarcsecond level. In 1995 March, Uitenbroek, Dupree, & Gilliland (1998) scanned the chromospheric disk of α Ori with GHRS and observed substantial changes in the prominent emission profiles of the Mg II UV resonance doublet. The aperture center scanned in perpendicular directions with successive steps of 27.5 mas, which is the apparent radius of the stellar disk in the optical. They found that the chromospheric emission from these lines reaches a diameter of at least 270 mas, about twice the size of the UV continuum (of ca. 120 mas), simultaneously obtained with the Faint Object Camera (FOC) by Gilliland & Dupree (1996). These spectra were however obtained through an aperture with a projected dimension of 200 mas square, which did not provide true spatial resolution on the chromospheric disk.

A further reduction of the slit size down to 25 mas by 100 mas is currently offered with the Space Telescope Imag-

ing Spectrograph (STIS). The brightness of α Ori in the near-UV is sufficient to provide the first truly spatially resolved spectra within realistic exposure times. Due to its proximity and supergiant size, Betelgeuse represents an exceptional target to study the kinematic structure (i.e. the spatial and temporal properties) of an extended supergiant chromosphere at the limits of modern technological capabilities. These new measurements also represent a further increase of the spectral resolution in the raster scans, from medium-resolution with GHRS to R=114,000 with STIS. Detailed profile changes of chromospheric emission lines can be observed with high spatial and spectral resolution. We present a study of selected emission line profiles in the near-UV of this cool prototypical supergiant, from which we infer properties of the chromospheric velocity structure with detailed radiative transport calculations. This spatial and temporal modeling places direct constraints on the chromospheric kinematics between 1998 January and 1999 March. Section 2 presents a brief description of the observations. In Sect. 3 we compare and discuss the variable morphology of unsaturated self-absorbed emission profiles across the UV disk. In Sect. 4 we model these profile changes for the Si I resonance line, with simultaneous downfalling and upflowing radial velocity structures observed in 1998 September. We discuss chromospheric turbulence and oscillation inferred from this detailed modeling. The conclusions are presented in Sect. 5.

2. OBSERVATIONS

A description of the STIS spectral scans used for the present study, with their wavelength and flux calibration, is provided in Lobel & Dupree (2000). For convenience we summarize the main properties of this data of HST proposal No. 7347. A spatial scan in the wavelength range between 2275 Å and 3120 Å was obtained on 1998 January 9, April 1, and September 24, and on 1999 March 28. The chromospheric disk was observed with an aperture size of 25 mas by 100 mas, by stepping in the cross-dispersion direction with the medium-resolution grating. This provided seven spatially resolved echelle spectra ($R{\sim}30{,}000$) in off-sets of 25 mas across the disk, over a single scan axis almost parallel (within $10°$) with the East-West direction. The scan axis of 1998 January was tilted by $-38.9°$ from E-W. Note that the stepping direction for the scan of 1998 September is reversed due to the $180°$ roll in the seasonal orientation of the HST. The designation of Target Position (TP) from intensity peakup for this scan is therefore spatially reversed for comparison with the other scans. An overview of the scan axes[1] with respect to the North direction in the plane of the sky is given in Sect. 4.2.3. The NUV-MAMA echelle line spread function and the absolute wavelength calibration for these spectra provide an accuracy within 1 pixel or 5 km s^{-1}. The signal to noise ratios (S/N) of the individual spectra vary across the disk because different (single) exposure times were applied. These ratios typically range from 40 at intensity peakup to 25 near the disk edge. The data of 1998 April were complemented by an additional scan with the high-resolution grating (R=114,000) in the wavelength range of 2666 Å to 2942 Å. These observations required a bigger slit size

of 63 mas by 200 mas, and the aperture center was placed in pointing offsets of 63 mas and 126 mas (left and right of intensity peakup). The wavelength calibration accuracy within one pixel corresponds to 1.3 km s^{-1}.

3. CHROMOSPHERIC EMISSION LINE PROFILES

3.1. *Line formation*

Numerous prominent emission lines from neutral and singly-ionized metals have been identified in the far- and near-UV spectrum. Carpenter et al. (1994) identified many blended Fe II and S I lines between 1200 Å and 2000 Å. These Fe II lines also dominate the spectrum from 2200 Å to 2800 Å (Brandt et al. 1995), resulting from the complex term structure of Fe II, which produces many blends between these lines, and with those of other elements. These profiles appear 'double-peaked' because a central absorption core forms when the transitions become sufficiently optically thick in the chromospheric line formation region. For instance, Fe II lines of several subordinate UV-multiplets (i.e. UV $60-64$) with large oscillator strength, display strongly intensity saturated self-reversals with central depressions below the intensity level of the line wings and the background continuum. On the other hand, the lines with lowest $\log(gf)$-values in these multiplets show single-peaked emission profiles in which self-absorption is hardly discernible with high spectral resolution and S/N [i.e. $\lambda2874.8$ (UV 61), $\lambda2716.7$ (UV 62), $\lambda2772.7$ (UV 63)].

Central self-reversals form when the line source function is not monotonically decreasing with distance from the base of the chromosphere, provided that the column density for the transition is sufficiently high (due to line opacity resulting from the chromospheric extension and thermodynamic conditions). This scattering core of optically thick emission lines removes photons, produced in the deeper chromosphere, from the line of sight in the upper layers where the source function decreases. The frequency dependent contribution functions to the relative emission intensity in the line profile are therefore strongly depth dependent and determined by the detailed velocity structure in the line formation region.

These complex profiles can be computed with radiative transfer through a well-constrained thermodynamic model of α Ori's extended chromosphere. A mean photospheric/chromospheric model of radial kinetic gas temperature, electron density, and microturbulence has been presented by Lobel & Dupree (2000), based on an elaborate fit procedure to the disk-integrated Hα profile, the Ca II K line, and the relative intensities and widths of the Mg II UV resonance doublet. This model reproduces the remarkable asymmetry observed for the latter lines. The intensity of the blue k emission component is partly reduced by a deep and narrow scattering core of the Mn I blend at 2794.8 Å. The frequency dependent contribution functions show how the line wings form below the central scattering core (see their Fig. 6). The relative contribution to the core flux increases in higher chromospheric layers with respect to the wings, which form deeper and closer to the chromospheric temperature rise. The emergent emission line profile is therefore dependent on the velocity structure in the for-

---

[1]For the positions of the slit with respect to images, simultaneously obtained in the UV with the FOC, see http://cfa-www.harvard.edu/cfa/ep/pressrel/alobel0100.html.

mation region of this scattering core. Photons moving toward the observer in a collapsing chromosphere encounter a larger opacity at the long-wavelength side of the line than the short-wavelength, and hence the blue wing appears stronger and the red wing fainter (Hummer & Rybicki 1968). A simple (parameterized) modeling of such asymmetric emission profiles of α Ori was carried out by Boesgaard (1979), based on Fe II lines with stronger blue components, observed around 3200 Å in 1970−75.

The component maxima of these double-peaked metal emission lines are observed to reverse over time. Brandt et al. (1995) observed reversals in Fe II λ2391.5 (UV 35), suggesting chromospheric inflow for 1988 March and outflow in 1989 January. Inflow was again observed in 1991 January (IUE), whereas both components had equal intensity in 1992 September (GHRS). The latter spectrum was analyzed by Carpenter & Robinson (1997) who inferred a correlation between the radial velocity of Fe II central reversals and computed line opacities. They detected an acceleration of the mean chromospheric velocity structure from rest to ~-7 km s^{-1}. The present STIS monitoring also reveals how these cores displace over time (by 4 to 8 km s^{-1}), which correlates with the strengthening of the red emission component when this core displaced bluewards between 1998 April and 1999 March (see Fig. 7 of Lobel & Dupree 2000). These observations point to recurrent upflows in the stellar chromosphere which may be linked with the 400−420 day variability period found by Dupree et al. (1987) from U-band photometry and Mg II fluxes, and by Smith, Patten, & Goldberg (1989) from photospheric radial velocity variations. A short review of chromospheric variability based on earlier spectral data is also given in Querci & Querci (1986).

3.2. *Spatial and temporal line component behavior*

Figure 1 shows the STIS raster scans obtained with the medium-resolution grating for our monitoring program. The profile changes observed in Fe II λ2868.874 (UV 61) (*dash-dotted lines*), Si I λ2516.12 (UV 1) (*solid lines*), and Fe II λ2402.6 (UV 36) (*dotted lines*) are shown in off-sets of 25 mas from intensity peakup (TP 0.0) on the chromospheric disk. Note that the Fe II λ2868.9 line intensity has been scaled up by a factor of 3 for comparison with the Si I profiles. These lines are investigated because their self-absorption cores are not intensity saturated. Intensity saturation is observed in α Ori for the stronger lines of these UV multiplets. It distorts the wing profiles of the reversals, thereby masking small changes in the Doppler position of this core. This is for instance observed in the wings of the wide and zero-flux self-absorption cores of Mg II h & k, which remain static between 1998 January and 1999 March.

In general, the scans of 1998 in Fig. 1 display stronger blue than red emission components, indicating downflow across the entire chromosphere. A closer inspection reveals that the component intensities are however not identical when scanning left and right of peakup position. For instance, in 1998 April the blue component exceeded the red much more at negative scan positions than for positive off-sets. The component ratio for both lines is noticeably larger at TP −0.025 than at +0.025. This difference results from the minimum in the Fe II self-reversal at TP

+0.025, which occurs $\sim$5 km s^{-1} blue-shifted with respect to TP −0.025. But the FWHM for the central core at TP +0.025 is also larger, which lowers the resulting intensity of its adjacent emission maxima. Although a similar asymmetry of component ratios is observed for the Si I line, clear differences in core position and width remain undetectable, which results from the deeper central core of this resonance line, which dips about 10 km s^{-1} bluewards of the Fe II centroid.

When scanning further off the disk in 1998 April we observe how the self-reversal of the Fe II λ2868 line becomes very weak at TP −0.075. A single-peaked emission profile appears, whereas the profile at TP +0.075 remains double-peaked. To test the influence of instrumental broadening we compare the profiles with the high-resolution scan. This raster scan was obtained immediately after the medium-resolution scan, but with a 63 mas by 200 mas aperture. The high-dispersion profiles of Fe II λ2868 are shown in Fig. 1 by the dashed drawn (noisily) lines. They correspond with the aperture placed off-limb at 0 mas (intensity peakup), ±63 mas, and ±126 mas. For comparison purposes we overplot these profiles at TPs ±0.050 and ±0.075, but recall that they sample a larger disk area and a wider spatial range. The absolute intensities are also scaled down for an effective comparison with the medium-resolution profiles. The component ratios in the high-resolution scan closely match (to within a few percent) the ratios of the medium-resolution scan. Notice also the component asymmetry at ±63 mas, and the same shape difference of a single emission line at −126 mas (shown at TP −0.075), but which is double-peaked at +126 mas (TP +0.075). This comparison reveals that the component ratios in the medium-resolution scans can be used to infer reliably the spatial structure of the chromospheric velocity field, because these emission lines are intrinsically sufficiently broad. The separation of both components exceeds 40 km s^{-1} (or at least 4 times $\Delta\lambda\simeq$0.09 Å), so that the difference between $R\sim$30,000 and R=114,000 has no appreciable effect on the observed line shapes.

The medium-resolution scan of 1998 September in Fig. 1 reveals that the asymmetry of component ratios at opposite sides of the chromospheric disk increases further. The blue component of the Si I line (*solid lines*) at TP +0.025 diminishes to below the intensity of its red emission component. This reversal is observed for both the Si I and Fe II lines, and extends farther out to TP +0.075. It suggests a reversal of the mean flow direction in the formation region of the self-absorption core, causing slight Doppler shifts of this core which strongly alter the emission maxima. In the next section we model these spatial reversals with small differences in the mean chromospheric velocity structure of the exposed disk area. This expanding trend, first detected at positive scan positions (West of peakup), is further observed in the raster scan of 1999 March. For this epoch the intensity maximum of the red component of the iron lines strongly exceeds the blue one for all positive scan positions, including TP 0.0. In the meantime, the intensity excess in the blue components has strongly decreased at the negative scan positions. This variability points to ongoing changes in the local chromospheric kinematics, extending further Eastwards across the chro-

mospheric disk.

Similar temporal and spatial evolutions are observed in Fig. 2 for other emission lines of Fe II λ2917.416 (UV 61) (*dotted lines*) and Al II] λ2669.166 (UV 1) (*solid lines*). The latter semiforbidden line also shows the spatial reversal of the component maxima when scanning from TP 0.0 to +0.025 in 1998 September. In 1999 March both lines display a strengthening of the red peak over the blue maximum at TP 0.0. However, component variations of lines that belong to the same multiplet are not necessarily identical. For example, Fe II λ2880.756 (*long dash-dotted lines*) is a transition with large oscillator strength of the same 61$^{\rm st}$ UV multiplet. This line permanently displays a stronger blue emission maximum (but is also blended with Cr II λ2880.863 which could distort its shape). Differences in profile changes are also observed among other lines with high and low $\log(gf)$-values that belong to the same multiplet. In general, the leading lines of a multiplet have deep and broad self-reversals, and display stronger blue emission maxima during our monitoring period. On the other hand, the unsaturated lines display a systematic evolution, which comprises spatial and temporal intensity reversals of their component maxima. Such lines are useful to track the detailed chromospheric kinematics. The component separation of core-saturated (i.e. strongly opacity broadened) lines of many Fe II multiplets typically exceeds 60 km s^{-1}, whereas the maxima of lines with unsaturated cores can be separated by less than 40 km s^{-1} (see Fig. 2). We note however that unblended lines with central absorption intensities above the level of the background continuum are rather scarce in the very crowded near-UV spectrum of α Ori. Two other examples are Fe II λ2759.336 (UV 32) and Fe II λ2449.739 (UV 34). These lines display morphologic changes very similar to the profiles shown in Fig. 1, including the sudden reduction of their component ratios from TP 0.0 to +0.025 in 1998 September. Similar behavior is observed in Fig. 2 for the somewhat stronger Fe II λ2984.831 line of UV 78 (*short dash-dotted lines*). Note that this line displays a stronger red component in 1999 March, which is also observed at TP 0.0 for Fe II λ2917 (*dotted lines*) and for the Al II line (*solid lines*). The weakly intensity saturated Fe II λ2402 line in Fig. 1 (*dotted lines*), with higher optical depth, also displays the spatial component reversal of 1998 September, which is observed for the two unsaturated lines in this Figure, and for the Al II line of Fig. 2.

In Fig. 3 we show the reversals between TPs 0.0 and +0.025 for these four lines. The Al II line (*solid lines in upper panels*) is drawn for two overlapping echelle orders. The close agreement confirms that instrumental noise remains small. Current STIS performance monitoring indicates that the E230M and E230H gratings are only affected by scattered light to 4% at 2500 Å (STScI 1999). Errorbars on the line intensities are also plotted for the Fe II λ2869 line (*dash-dotted lines in upper panels*), and the weaker Si I line (*solid lines in lower panels*). The errorbars are provided by the STIS calibration pipeline and are mainly determined by the accuracy of the absolute sensitivity calibration of the E230M grating and of the aperture throughput, and by the bias and background subtractions in case of low intensities. We observe these reversals however near disk center for which the spectra have good S/N$\sim$40, with global count rates $\sim$2000 s^{-1}. The spatial intensity changes in the emission components exceed these errorbars, which indicates that the systematic differences result from changes in the line formation conditions across the chromospheric disk.

In summary, we observe systematic profile changes in weak emission lines of various species, that are formed in Betelgeuse's chromosphere. The line shapes are characterized by asymmetries which vary with the chromospheric kinematics. Spatially resolved observations of selected (unblended and unsaturated) lines reveal that complex chromospheric velocity structures are present during these variability phases.

4. CHROMOSPHERIC MODELING

4.1. *LTE synthesis*

The upper panel of Fig. 4 shows a portion of Betelgeuse's near-UV spectrum (*thick solid lines*), observed between 2735 Å and 2750 Å. This medium-resolution spectrum was obtained at intensity peakup (TP 0.0) in 1998 September. The region between 2736 Å and 2745 Å is obtained from two overlapping echelle orders, for which the emergent fluxes closely match. This region is typical for the star's UV spectrum which displays a forest of emission peaks, crossed by broad zero-flux absorption troughs that are seen against an apparent mean level of the UV background. These zero-flux cores have been identified in Brandt et al. (1995), and result from prominent self-reversals of many blended Fe II lines, mostly of UV-multiplets 62 and 63.

The synthetic spectrum for this region is shown by the thin drawn solid line. For this computation we apply the mean thermodynamic model atmosphere of Lobel & Dupree (2000). This model has been determined from NLTE fits to the Hα profile, observed in 1993 February. The normalized core depth of Hα was equal to within 5% of the depth observed in 1998 October. The spectrum in Fig. 4 is however computed for LTE conditions in plane-parallel geometry. This is because a detailed NLTE synthesis would require much more elaborate computations that solve the radiative transfer and rate equations for the very complex Fe II atom. This is outside the scope of our present study which merely tries to identify the strongest spectral features from these approximate fits. We find that an LTE synthesis already meets this goal very closely. This spectral region is well-matched by only considering Fe I - and Fe II-lines in the synthesis, shown by the dotted line (*upper panel*). The positions of the strongest Fe II lines are marked in the stellar rest frame. The lower energy levels of these lines do not exceed $\sim$3 eV, with $\log(gf)$-values typically above -1. The iron spectrum fits the majority of the observed strong spectral features. The synthetic spectrum computed with all atomic species is shown by the thin solid line. Differences with the iron spectrum remain limited, although some weaker absorption cores in the observed spectrum are also identified as Cr II lines at the indicated wavelengths. The line list and the atomic line data are available from Kurucz website (1998)[2]. Note that the current atomic data produces unobserved strong iron emission lines, for example Fe I λ2737.633 and Fe II

---

[2]URL at http:/kurucz/linelists.html

$\lambda 2744.897$. The $\log(gf)$-values of the transitions at $\lambda 2737$ and at $\lambda 2745$ are computed to be too strong (respectively -1.801 and -1.727). Note however that the small $\log(gf)$-value of -0.939, given in Fuhr, Martin & Wiese (1988) for the Fe II $\lambda 2741.394$ line, produces an emission line intensity which matches the observations.

On the other hand, our spectral synthesis correctly reproduces the strong self-absorption cores observed in the leading lines of subordinate iron multiplets (i.e. Fe II $\lambda 2739.548$ with $\log(gf)=0.233$), which suggests that these f-values are appropriate. The broad overlapping line wings occasionally match the observed near-UV background fluxes (i.e. near 2748 Å). Note that Carpenter et al. (1994) confirmed with GHRS spectra that this background, first detected with IUE, is a true continuum which is not due to scattering inside the spectrograph. They also argued that it appears to originate in the chromosphere at temperatures ranging from $3000-5000$ K, in agreement with our semi-empirical chromospheric model.

It is of note that the near-UV fluxes of Betelgeuse also vary slightly over different regions of the inner chromospheric disk. Gilliland & Dupree (1996) found excess emission in the radial intensity distribution observed in the near-UV in 1995 March. This resulted from a brighter feature seen in the SW disk quadrant. This 'spot' was observed within 25 mas of the disk center. Similar, but not identical, patterns in the UV-continuum brightness are also observed within ~ 30 mas of intensity maximum, in dithered FOC images that are simultaneously monitored with the STIS spectra (Dupree, Lobel, & Gilliland 1999). We conjecture that these UV-continuum patterns are related to the asymmetric brightness distributions observed by Young et al. (2000) with optical interferometry. They suggest that the dominant TiO opacity in the optical is very sensitive to small differences in local thermodynamic conditions across the photosphere, because no brightness asymmetries have been measured in the near-IR where TiO opacity is almost absent (R. Kurucz, 2000, private communication). Probably, a similar temperature/density dependence for the chromospheric continuum level can alter the emergent near-UV fluxes that are observed across the chromospheric disk.

The LTE spectral synthesis is performed through the stellar chromosphere to check for possible blends in the profile of the lines we discussed in the previous Section. The lower panels of Fig. 4 show the computed LTE spectrum near the Si I $\lambda 2516$ line (*panel left*) and the Al II] $\lambda 2669$ line (*panel right*). The observed profiles of 1998 September are boldly drawn. They are shown for TP 0.0 (*solid lines*) and TP $+0.025$ (*dashed lines*), and display the remarkable spatial reversal of their component maxima. Two Al II profiles are drawn for each pointing position, obtained from two overlapping echelle orders. The computed profiles are shown by the thin dash-dotted lines. The Si I resonance line becomes strongly self-absorbed because of its high $\log(gf)$-value (0.241) and very small lower energy level. The Al II is a zero electron-volt semiforbidden transition with a weaker self-reversal due to its smaller optical thickness and low $\log(gf)$-value of -4.69. After broadening the computed Si I profile with the instrumental resolution, and with a total value for $v\sin i$ and macroturbulence of 9 ± 1 km s^{-1}, we find that the shape of the self-absorption

core (*thin drawn solid line*) closely matches the observed core profiles. The width of this scattering core is strongly dependent on the microturbulence velocity profile in the chromosphere, which ranges up to 19 km s^{-1} in our model.

The component maxima of the computed profiles assume equal intensities because a hydrostatic model chromosphere is applied. This reveals that both lines are not blended with other strong chromospheric emission lines. However, the spectral synthesis yields weak emission lines of Fe II $\lambda 2516.407$ and of Fe I $\lambda 2516.571$. Both iron lines appear unobserved when comparing the computed (and broadened) profile with the long-wavelength wing of the observed profiles. Their $\log(gf)$-values are predicted to be too high, similar to the iron lines in the upper panel of this Figure. This is also found for the predicted Cr II line at $\lambda 2668.707$ with high $\log(gf)=-0.524$. The strong emission components are not observed, but its deep self-reversal can be identified with a broad absorption core which is observed at the short-wavelength side of the Al II line.

Carpenter & Robinson (1997) measured highly supersonic average chromospheric turbulent velocities in the range of $31-35$ km s^{-1} from the Doppler FWHM of intercombination lines of C II and Si II, and from fluorescent Co II and Fe II lines. These values are however based on the assumption that these emission lines can be considered as optically thin, and that the broadening is controlled by turbulence rather than opacity effects. Our spectral synthesis and detailed radiative transfer modeling reveals however that macroturbulence is not the main broadening mechanism and that chromospheric emission lines in α Ori are considerably opacity broadened. Their high macrobroadening values are therefore strongly overestimated since the line widths are determined by various other broadening mechanisms. It is to be remembered that the FWHM of a spectral line is determined by the thermal motions of the gas *and* the (projected) *micro*turbulence velocity when radiative transfer effects are important. Next to these effects, the lines shape can broaden further by *macro*broadening. The latter conserves the total line flux, and can result from large-scale mass movements, stellar rotation ($v\sin i$), and the instrumental dispersion. In the lower panel of Fig. 4 (*right*) we compute that about half of the observed FWHM of the Al II $\lambda 2669$ intercombination line (*bold lines*) results by radiative transport in the chromospheric formation region (*thin dash-dotted line*), whereas the remainder of the line width can be ascribed to macrobroadening. Since the rotational broadening for Betelgeuse and the instrumental broadening are small we compute a value of 9 km s^{-1} for the large-scale (macroturbulent) velocity for convolution with the predicted spectrum to obtain an overall best match with the observed near-UV spectrum (*upper panel*).

Although the C II] lines do not display self-absorbed central cores as the Al II] line, it has been pointed out that these lines should *not* be considered as optically thin transitions. Judge & Carpenter (1998) presented a discussion about effects of radiative transfer on the C II intercombination lines. They assumed that these lines are 'effectively' optically thin, and applied the 'mean escape probability approximation' to determine the electron density in the mean formation region. They derive $N_e \simeq 10^{8.3}$ cm^{-3},

which is about a factor of ten larger than in our semi-empirical model (Lobel & Dupree 2000), which is based on detailed radiative transfer modeling of Hα, Mg II h & k, and TiO bandheads. However, Judge & Carpenter (1998) also conclude that the optical depth inferred from their line ratio estimates are high enough in the chromosphere to influence these ratios, and thereby "render all conclusions based upon the assumption of optically thin line formation invalid for these lines". It has been known for some time that this assumption yields very different values for the chromospheric electron density. For example, Stencel et al. (1981) measure $\sim2\times10^8$, $\sim5\times10^7$, and $\sim1\times10^7$ cm^{-3}, for the three line ratios, assuming a temperature of 10^4 K in the line formation region. Comparative studies by Byrne et al. (1988) demonstrated that the relative intensities of the C II] lines are variable between exposures with IUE. They noted that electron densities derived from different line ratios were incompatible, and reported evidence of variation in the line profile from one exposure to another. This variability points to line broadening mechanisms determined by important radiative transport effects in these transitions.

4.2. Detailed NLTE modeling

The profile of the Si I $\lambda2516$ line also shows strong temporal changes besides the spatial variations discussed above. For instance, in 1992 the GHRS disk-integrated self-absorption core revealed a blue-shift by ~10 km s^{-1}, compared with the 1998-99 STIS scans. Its red component maximum strongly exceeded the blue one, while the former became much weaker in 1998-99. Lobel & Dupree (2000) determined a mean chromospheric velocity structure from this line profile in 1992, which accelerates from rest to about -4 km s^{-1}. The Si I profiles of 1998 January and April in Fig. 1 indicate inflow in the core formation region since the blue component exceeds the red. But the spatial reversal observed at TP +0.025 in 1998 September (see Fig. 3) indicates the local alteration of this downflow into upflow. We infer the corresponding kinematic structure in the chromosphere from a refined NLTE modeling of these variable component ratios, based on the thermodynamic model of Lobel & Dupree (2000).

4.2.1. Spatially resolved modeling

We utilize the SMULTI code (Harper 1994). It computes emergent line profiles in moving media and accounts for their formation in spherical geometry and non-LTE conditions. The equation of state considers the ionization stages of hydrogen and helium (for solar abundance values), and the electron pressure. The statistical equilibrium and rate equations are solved for two adjacent ionization stages of the species (with a user defined abundance) for which we model the spectral line shape with detailed radiative transport calculations. The code outputs the line flux, the ionization fraction for the considered element, together with its departure coefficients from LTE for the ionization and excitation fractions per model layer and atomic energy level. The non-LTE equilibria are very sensitive to the kinetic temperature and the local electron density (N_e) adopted in the model atmosphere. The model is obtained by semi-empirically varying both structures with height, until the 'best match' is obtained with the observed line

flux and shape. The computation of emission lines formed in the chromosphere with spherical geometry is critically dependent on N_e, because the chromosphere is predominantly cooled by mechanisms which depend linearly on N_e per gram (electron collisional excitation of neutral and singly ionized species and H$^-$ recombination; see Harper 1994). The modeling method is based on the mass conservation technique (Eq. (2) of Harper 1994), which yields slightly different temperature, gas-density, and -pressure structures for the different phases, with variable mass-loss rates. Thermodynamic models which also list various quantities like column mass, optical depth, mass density, number densities of H I and H II, total gas pressure, electron pressure, turbulent pressure, pressure scale height, can be obtained in electronic form from the authors.

The term structure of the silicon atom is sufficiently simple (as opposed to iron), to converge the population densities throughout an extended model of the chromosphere, within acceptable runtimes. A Si model atom with 12 energy levels and the continuum is applied. We solve the radiative transfer and statistical equilibrium equations for 6 line transitions and 9 fixed continua. The line at $\lambda2516$ has a common upper level (χ_{up}=4.953 eV, g=5) with the lines at $\lambda2506$ and at $\lambda2970$ ($3s^2\,3p\,4s\ ^3P^o{\rightarrow}3s^2\,3p^2\ ^3P$). The former is a prominent emission line in the spectra, but the latter has not been identified, possibly due to blends with Fe I lines (Brandt et al. 1995). Three other transitions connect the level at χ_{up}=4.929 eV (g=3) with the same lower levels of the above listed lines. The intrinsically weakest line at $\lambda2987$ is observed as a strong emission line without a self-reversal. The two other transitions at $\lambda2519$ and at $\lambda2528$ with oscillator strengths ~20 times larger, are strongly self-absorbed, and display weak emission components against the near-UV background. Carpenter et al. (1988) showed that the line at $\lambda2516$ (e.g. also observed in the M3 giant γ Cru) is a fluorescent line whose upper level is populated by a fluorescent Fe II line at $\lambda2506.8$, which pumps the Si I line at $\lambda2506.9$. This could explain why the latter line appears so strongly in emission, whereas the line at $\lambda2519$, with otherwise comparable oscillator strength and transition probability (A_{ul}), does not. The present modeling procedure does not readily account for changes in the branching ratios due to pumping, or by photon conversions due to this Fe II blend. Such changes by extra photo-excitation on the emergent intensity ratios of these lines, sharing the same upper level, are however not relevant to fit *relative* intensities of the component maxima in the Si I $\lambda2516$ line. Fluorescence in this transition enhances both components equally, which can be accounted for by scaling up the predicted profile.

The upper left panel of Fig. 5 shows the best fit (*thin solid line*) to the Si I line observed at TP 0.0 in 1998 September (*bold solid line*). The computed profiles in this Figure are spatially resolved by summing the intensity contributions from light rays that propagate parallel to the line of sight, and cross the projected surface area within the field of view, for each aperture position on the chromospheric disk. This integration is performed along the width (25 mas) and height (100 mas) of the slit, placed in off-sets of 25 mas from the center of our model atmosphere. These fluxes are multiplied by the geometric weighting factors to account for the spherical curvature of the atmosphere (or

the path length for every ray within the sector of the chromospheric model included in the STIS aperture), to yield the emergent spatial line intensities. For these computations the photospheric core radius of 27.5 mas is set to $R_\star$=700 $R_\odot$, where τ_{5000}=1. There are 21 model layers below this point (where $T\simeq T_{\text{eff}}$), with the deepest layer located at 8.6×10^{11} cm ($\sim$12 $R_\odot$ or 0.017 $R_\star$) below the formation region of the photospheric continuum. The radiative transport is solved for 5 rays intersecting this core, whereas light rays that graze the photospheric core are computed throughout the outer 50 layers above the core radius. In these chromospheric layers the kinetic temperature T increases from a minimum of 2769 K to a maximum of 5443 K, then decreases outwards to $\sim$3000 K at a height of 9.3 $R_\star$. For the *Hipparcos* (ESA 1997) distance of 131 pc to α Ori, this height corresponds to $\sim$250 mas, which is beyond the outermost radius of $\pm$87.5 mas (at TPs $\pm$0.075) of our raster scan with the 25 mas aperture. Therefore, light rays that *start* from layers above 87.5 mas (outside the field of view) do not contribute to the intensity integration. These layers of course do contribute farther out to passing rays that start deeper, inside the projected slit area. Note that the pointing jitter for these observations in the HST fine-lock mode remains typically below 3.5 mas, which is sufficiently small with respect to the slit size to enable an effective comparison of the emergent line intensities with scan position.

The computed profile of Si I λ2516 at TP 0.0 in Fig. 5 matches the observed line shape with a downfalling mean velocity structure, shown in the upper right-hand panel (*solid line*). We compute that a radial acceleration of this inflow, from rest to 1.4 km s^{-1} at 1.85 $R_\star$ above the photospheric radius, produces the observed intensity ratio of the line components within their errorbars at central intensity. An increase of the downflow velocity by 1.6 km s^{-1} (*dotted line* for a terminal inflow velocity of 3 km s^{-1}) increases this ratio by $\sim$25 %, which indicates that the detailed Si I line shape serves as an accurate velocity indicator in the chromosphere. Note that there is slight movement of the central core depending on the terminal velocity, but the line asymmetry is more pronounced and more easily measured. A velocity structure for which the inflow accelerates slowly (*long dash-dotted line*) to 1.4 km s^{-1} produces a blue emission component that is $\sim$20% too weak compared to a velocity structure which steeply accelerates in the deeper chromospheric layers. The latter mean velocity structure provides the best match with the profile observed at TP 0.0. The contribution from the photospheric continuum becomes largest with respect to the line flux because the slit width mainly samples light rays that start inside the photospheric core. The rays that contribute along the slit height also include grazing rays out to 50 mas. On the other hand, the off-star scan positions chiefly integrate rays that graze the inner core. This adds little or no photospheric background continuum, which is shown in the lower panels of Fig. 5 by the thin drawn solid lines. Note that we compute this background with the Uppsala opacity package in spherical geometry as well. The photospheric background flux is dominated by bf-opacity of H and H$^-$, whereas in the chromosphere the continua of Al and Mg are important (i.e. the strong bound-free opacity edge of Mg I at 2513 Å), besides the electron opacity. For a gas

of solar abundance we compute that hydrogen is partially ionized up to 35 % near the temperature maximum.

Our detailed modeling procedure requires a redshift for the synthetic profiles of +18.3 km s^{-1} to provide a best global fit to the line shape observed at TP 0.0. The profiles are computed in the stellar rest frame, and have to be corrected for the stellar radial velocity in the heliocentric frame. The computed profiles in Fig. 5 are plotted with a redshift of +18.3 km s^{-1}, for all the scan positions. It is of note however that this value does not equal the center-of-mass velocity of α Ori. Between 1998 January and September we detect redshifts of $\sim$+8 km s^{-1} in the scattering cores of Fe II λ2392 and Si I λ2516, which are typical for most emission lines in the near-UV spectrum (Lobel & Dupree 2000, see Sect. 6 of). This results from mean chromospheric mass movements. For example, in 1992 September the central core of Si I λ2516 strongly blueshifted during a phase of global chromospheric expansion, and which enhanced its long wavelength emission component. Chromospheric emission lines exhibit temporal variations of radial velocity that are comparable to the amplitude of the photospheric radial velocity curve. An overview of optical radial velocity studies for α Ori is given in Smith, Patten, & Goldberg (1989).

These raster scans further reveal that the intensity of the background emission near 2500 Å reduces almost linearly from TP +0.025 to TP +0.075, about halving at each subsequent scan position. This dimming is smaller in bright emission lines (or in their components) observed for this wavelength region. It results in brighter line emission maxima (i.e. they show limb-brightening) with respect to the background level when scanning off the disk. For the Si I line of Fig. 5 this ratio changes from $\sim$4 at TP 0.0 to $\sim$7 at TPs $\pm$0.075. This distribution of emergent line intensities is well matched with our mean thermodynamic model atmosphere. The model also reproduces the gradual weakening observed in the depth of self-absorption cores with respect to the off-star background levels. This spatial behavior is for instance clearly noticeable in the unsaturated core of the Fe II line at 2868 Å of Fig. 1. It results from the decrease in column density of the scattering material in the upper chromosphere with larger viewing angles. This effect is reproduced in Fig. 5 with our spatially resolved radiative transfer calculations.

4.2.2. *Projection effect*

Another important effect in modeling Betelgeuse's chromospheric kinematics is the geometric projection of its (complex) wind structure when scanning towards the limb. For the ideal case of a radially expanding (contracting) wind, which sustains a single velocity with distance, the Doppler position of the self-reversal is displaced from shorter (longer) wavelengths towards the rest-frequency of the line near the limb. Near the disk edge the central core forms in flow directions that are nearly perpendicular to the line of sight, whereas at disk center its formation chiefly samples the wind flow parallel with this line. Through this projection effect, emergent line profiles become more symmetric when scanning closer to the limb. The profile at peakup position (at or near the disk center) probes the radial component of the outflow (inflow) velocity because this self-absorption core mainly forms in front

of the disk, suppressing the resulting blue (red) emission component according the magnitude and direction of the mean flow velocity.

In reality this ideal scenario is severely complicated in several ways. The size of the aperture still covers about a quarter of the UV-disk area, so that towards opposite ends of the slit, light rays are integrated that emerge from radial outflow (or inflow) with reversed directions, perpendicular to the line of sight on either side of the chromospheric front hemisphere. Although the intensity contribution from these rays is smaller than for rays collected near the middle of the aperture, they reduce the asymmetry of the integrated line profile. This effect diminishes when scanning off the disk where the field of view samples a more uniform (tangential) flow direction, but where the line intensity (and S/N) diminishes as well. Further complications arise from probable velocity variations along the radial wind profile in the star's extended chromosphere. The detailed wind structure may accelerate and/or decelerate with distance above the photosphere. The higher inflow velocity at larger distance in Fig. 5 causes the strong component asymmetry computed for TP 0.0 (*thin solid line*), which is observed in 1998 April (*bold dash-dotted line*) and 1998 September (*bold solid line*). For TPs ±0.050 and ±0.075 the asymmetry in the computed profiles reduces noticeably due to the geometric projection. This effect is observed at the negative scan positions, in agreement with our spatially resolved modeling. But the profiles observed at positive scan positions clearly do not match this model with downflow. These off-star component maxima in 1998 September reverse with respect to TP 0.0. The emission maxima at the positive scan positions are best fit (*thin dash-dotted lines*) with an outflowing (mean) velocity of 0.5 km s^{-1}, shown by the dash-dotted line in the upper right-hand panel. Note that it closely fits the relative and absolute component intensities at TPs +0.025 and +0.075. However, the absolute intensity of the profile predicted for TP +0.050 is somewhat too strong. This can result from the mean thermodynamic model we apply for all scan positions. Small spatial differences across the chromosphere in the local kinetic temperature or electron density may account for small differences in the absolute intensity distribution of the line. This is not unexpected, since images of Betelgeuse display chromospheric surface features. On the other hand, the relative intensity distribution in the line components chiefly depends on the detailed chromospheric velocity structure, which is reproduced with this spatially resolved modeling.

Further simulations reveal that the systematic and prominent component reversal from TP 0.0 to TP +0.025 cannot be modeled with complex non-monotonic radial velocity structures that collapse and expand with depth. The reversals occur too close to the inner (photospheric) disk radius, because these profiles mainly sample chromospheric mass movements parallel to our line of sight. This excludes the possibility that reversals can result from a combination of the projection effect and a *unique* but non-monotonic radial velocity structure. In principle, such combination can produce component reversals for the outer scan positions, which sample a more uni-directional flow in the field-of-view. However, for the inner scan positions appreciable contributions occur from light rays cross-

ing opposite flow directions on either side of the front hemisphere, when a unique (but complex) radial velocity structure is assumed. Such contributions render the integrated profiles more symmetric, contrary to what is observed at TPs 0.0 and +0.025. Our modeling shows that the reversals, observed at these inner scan positions, can only be caused by an inversion in the mean radial flow direction between these scan positions. This implies that the chromosphere assumes an inherently non-radial velocity structure in September 1998.

4.2.3. *Chromospheric kinematics*

Figure 6 shows a three-dimensional schematic representation of the chromospheric velocity structure, inferred from the spatially resolved observations and the detailed line profile modeling. The dashed lines mark the aperture positions with respect to the photospheric hemisphere, drawn by the dotted circles which contour surface areas of 30° latitude and longitude. The size and direction of the arrows indicate the radial speed and flow direction above a surface area for the chromospheric fluid in the front hemisphere. This radial velocity structure is represented at four depths in the chromosphere. It clearly illustrates the projection effect for grazing light rays that cross the chromosphere at different locations within the aperture, and for different scan positions of the latter on the chromospheric disk. The chromospheric velocity pattern of 1998 January shows a decelerating mean downflow since the blue component maxima of unsaturated lines are stronger across the disk. This observed line asymmetry slightly enhances for negative scan positions in 1998 April, which is represented by a somewhat stronger downflow on the Eastern (left-hand) hemisphere. The reversals discussed above in the component maxima of unsaturated lines, observed from TP 0.0 to +0.025 in 1998 September, are represented by outflow in the deeper chromospheric layers on the Western (right-hand) hemisphere (lower left graph). This local upflow occurs inside a larger collapsing chromospheric envelope. The mean downflow in this outer envelope is observed through the stronger blue components of many lines with saturated scattering cores (like Fe II $\lambda2881$ and Fe II $\lambda2985$ in Fig. 2) that sample a bigger and more extended chromospheric volume in the line of sight, with higher optical depths than the cores of the unsaturated lines. This global chromospheric inflow strongly decelerates or begins to reverse in 1999 March when much more symmetric line profiles are observed. The reduction of the line asymmetry extends further towards the negative scan positions, and is represented by outflow from deeper layers, extending higher up in the chromosphere towards the Eastern hemisphere (lower right-hand graph). This systematic evolution indicates a stratified flow that is not strictly radial in Betelgeuse's extended chromosphere, and which reverses from a global contraction into expansion during this 15 months monitoring period.

4.2.4. *Chromospheric turbulence*

The difference we determine for 1998 September of mean inflow of 1.4 km s^{-1} at TP 0.0 and mean outflow of 0.5 km s^{-1} at TP +0.025 is small, since it does not exceed the isothermal sound speed of ~7 km s^{-1} in the chromosphere. However, the Doppler position of the Si I

self-absorption core samples the depth-integrated fluid velocity. Local flow velocities in the chromosphere can be much higher on a length scale smaller than the mean formation region for this scattering core, but which become averaged out by this depth integral. This is illustrated by the small distance of only 0.015 $R_\star$ a 'mean' upflow with 0.5 km s^{-1} would travel between 1998 September and 1999 March. It is therefore relevant to compare these average fluid velocities with the large value for the macrobroadening of 9±1 km s^{-1}, required to derive the correct line width from the predicted (NLTE) profile, after correcting for the instrumental spectral resolution. This value is also well-constrained because higher values would produce self-reversals that are too broad and too shallow for the detailed fits of Fig. 5. Boesgaard (1979) also determined that the observed profile shapes rule out large-scale non-thermal motion of more than 10 km s^{-1}. Since the $v\sin i$-value for this evolved supergiant is expected not to exceed $\sim$5 km s^{-1}, this large macrobroadening-value can in part result from actual large-scale turbulent movements in the chromosphere. Strong large-scale up- and downflow in Betelgeuse's chromosphere cannot be ruled out because Lobel & Dupree (2000) determined a value of 12±0.5 km s^{-1} for the photospheric macrobroadening from single and unblended absorption lines observed with very high spectral resolution around 10800 Å. These metal lines also provided an accurate value of 2±1 km s^{-1} for the projected microturbulence velocity in the photosphere. The large difference between the photospheric microturbulence of $\sim$2 km s^{-1} and a macroturbulence velocity of 16±9 km s^{-1}, has also been observed for the M1.5 Iab supergiant α Sco by de Koter, de Jager, & Nieuwenhuijzen (1988).

The variable brightness patterns observed by Dupree, Lobel, & Gilliland (1999) in the near-UV of Betelgeuse can result from large-scale convective movements in the deeper photosphere which penetrate the lower chromosphere. Convection plumes that occasionally overshoot the chromospheric temperature minimum will cause small differences in the local kinetic temperature and produce the observed flux variations. Most importantly, our best fits to the line width observed near the disk center and near the limb in Fig. 5 require a constant value for the velocity of this 'chromospheric macroturbulence', projected in the line of sight. For every scan position we convolve with the same Gaussian macrobroadening profile. It indicates that these large-scale turbulent motions remain isotropic or angle independent across the chromosphere. This constant value for macrobroadening is also measured in the scan of 1998 January (see Fig. 1), when the scan axis was tilted by $-39°$ with respect to the East-West direction. A clear change of the total line width caused by the different slit orientation is not apparent, which indicates that the observed macrobroadening is not determined by high projected rotation velocities ($v\sin i$-values) in this line. The spatial invariance for this broadening, observed in these optically thick emission lines, appears to be linked with an isotropic and uniform large-scale velocity field in the star's extended chromosphere. The limited (subsonic) changes we observe in the average fluid velocity across the chromosphere, and this invariable macro-turbulence field could indicate that these small velocities are interdependent or

originate from the same type of velocity field. In other words, subsonic non-radial oscillations of the entire chromosphere may produce uniform (macroturbulent) eddies with similar or higher velocities on smaller length scales (e.g. like shaking a 'snowglobe'). The latter are clearly not resolved with the 25 mas by 100 mas aperture since the observed line broadening remains constant across the disk. This observation strongly suggests that macro-turbulence in Betelgeuse's *chromosphere* cannot be interpreted as due to the spatial inhomogeneity of a large-scale granular velocity field that consists of a few convection cells.

Energy cascading from large-scale eddies onto smaller length-scales with higher velocities, under gravitational confinement, is also consistent with the highly supersonic microturbulence velocities in our chromospheric model. These velocities are required to match the shape and width of the self-absorption core, or the separation of the emission line components (see Figs. 4 & 5). The core forms on average higher in the chromosphere than the emission line wings, where this small-scale velocity field also increases in our model. It is of note that de Jager, Lobel, & Israelian (1997) have shown that the supersonic photospheric microturbulence observed for the hotter and more luminous supergiant ρ Cas (F2−G Ia$^+$) can be mimicked with hot and thin sheet-like layers, produced by the wakes of outward propagating shock wave trains. The hydrodynamic motions in these shocked layers are small (with Machnumbers close to unity), but their high temperatures account for the observed extra thermal line broadening that mimics a strong micro-'turbulence'.

For α Sco A de Jager et al. (1991) computed that these shock waves have average wavelengths of about twice the local density scale height, which is much longer than the correlation length for the small-scale density/temperature fluctuations affecting the population densities in the radiative transfer (e.g. Hegmann & Kegel 2000). A microturbulent 'filter function' provides the fraction of kinetic energy of the large-scale motion field at a given wavelength which contributes to the microturbulent broadening of a spectral line (de Jager 1992). Based on the line formation function, and the field of temperature fluctuations produced in the wakes of these shock trains, an integral function is obtained from which the atmospheric *quasi-microturbulence* can be computed. It is of note that in (limited) 3D simulations of compressible turbulence Porter et al. (1997) demonstrated that shock waves develop from an initially uniform state which has been perturbed by randomly oriented, isentropic, sinusoidal sound waves. Many shock surfaces develop in the flow and intersect along lines from which slip surfaces, or sheets of vorticity emanate. Since a field of outward propagating sound waves is expected to be generated by the deeper convection zones in cool massive stars, these 3D shock wave collisions can develop into a large number of vortex tubes in higher layers. Possibly they can produce the high microturbulence velocities we observe in Betelgeuse's chromosphere?

Chromospheric Alvén wave heating in α Ori was discussed by Hartmann & Avrett (1984). Airapetian et al. (2000) recently discussed the results of 2.5 MHD modeling work and concluded that a high mass-loss rate of 10^{-6} $M_\odot\,yr^{-1}$ can be explained if the magnetic field is several hundred gauss in the lower chromosphere. How-

ever, observational indications for such large magnetic field strengths have presently not been demonstrated.

Different types of detailed non-magnetic hydrodynamic calculations have been presented with respect to heating and dynamics of low-gravity atmospheres. Cuntz (1997) assumes the (stochastic) generation of acoustic waves by the subphotospheric convection zone that propagate into the chromosphere. It is unclear how acoustic waves alone can create the global downfall for the very extended chromosphere of Betelgeuse (more than seven times $R_\star$), as we observe in our STIS spectra of 1998. Bowen (1988) computed the development of large-scale mass motions in circumstellar environments which result from photospheric pulsations (or piston action) in AGB stars. These models do not propagate into a hotter chromosphere (as exists for Betelgeuse), and rely on radiation pressure on dust grains to accelerate the circumstellar gas. Betelgeuse's chromosphere is too hot for dust nucleation (Lobel & Dupree 2000). We suggest that further hydrodynamic modeling should combine a cyclic acceleration of the deeper atmosphere by photospheric pulsations which strongly enhance the atmospheric density scale height, with the generation of gravity waves that can produce sound waves and dissipating shocks at large distance from the surface. We think that the opportunity exists to compute such models for the very extended and dynamic chromosphere of Betelgeuse, but that has not yet been accomplished.

Whether α Ori's extended chromosphere results from heating by viscous dissipation of turbulent energy, small-scale pressure waves and/or periodic photospheric accelerations, linked with the non-radial chromospheric movements we presently detect, can only be addressed when the source of these large-scale vibrations has been identified.

4.2.5. *Chromospheric non-radial oscillation*

Semi-regular pulsation of stellar photospheres is traditionally attributed to intermode beating of different radial pulsation frequencies, producing a long 'quasi'-periodicity, observed in Betelgeuse (SRc). However, attempts by Smith, Patten, & Goldberg (1989) to fit its radial velocity (RV) curve with single- and double-mode sinusoids did not provide any satisfactory explanation (for a discussion see their Fig. 4).

The long quasi-periodicity of light- and RV-curve of Betelgeuse is observed in other cool pulsating massive (Ia and Iab) supergiants as well. For example, for the yellow hypergiant ρ Cas (Ia$^+$), with $R_\star \simeq 400 \pm 100\, R_\odot$, Lobel et al. (1994) demonstrated from an improved Baade-Wesselink pulsation test that photospheric *radial* pulsations must be discarded to combine $T_{\rm eff}$-changes with the co-eval RV- and light-curve, observed over a complete variability period. Though the opacity, energetics, and atmospheric structure of ρ Cas is likely quite different than α Ori due to differences in the effective temperatures and evolutionary state of these two stars. Goldberg (1984) noted the absence of a one-to-one correlation between short-term radial velocity and visual brightness variations in Betelgeuse, which makes it apparent that these changes are not global in nature.

Velocities associated with non-radial oscillation are expected to have a horizontal component as well. For adiabatic boundary conditions, the ratio of horizontal to ver-

tical displacements is equal to 1 over the dimensionless pulsation frequency squared (Cox 1980). For red supergiants this number is very small, suggesting that the component of vertical motions is very small. This is particularly true for gravity modes. The small radial velocities we measure from the emission line asymmetries across the chromospheric disk (not in excess of $2\,{\rm km\,s^{-1}}$ between simultaneous up- and downflows), compared to the horizontal velocity required to extend the upflow in the lower chromosphere from the Western towards the Eastern hemisphere (thus at least over one stellar radius) between 1998 September and 1999 March, appears to support the g-mode hypothesis.

Hayes (1980, 1981, 1984) provided other observational indications for local non-radial pulsation of Betelgeuse's atmosphere. Long-term monitoring of linear polarization changes reveals the presence of surface features which likely result from the waxing and waning of large-scale convective cells. Gravity modes with $l=0$ (radial motion) or $l=1$ (dipole motion) do not distort the star's spherical shape and can therefore be discounted to explain the changes of net polarization which occur over intervals of about one year. He also found that the changes of the Q and U Stokes parameters are not conform with polarization changes expected for a single *global* pulsation mode. However, *local* non-radial pulsations provide a means of producing the requisite asymmetry. The ordered changes of polarization position angle can be explained by the changes in the orientation of a few large-scale surface elements (i.e. convection cells) which grow and fade over time, while migrating randomly across the stellar disk. Preliminary hydrodynamic 3D-simulations of giant granules in the photosphere of an entire red supergiant are presented in Freytag (2000).

Very high l-modes are not expected for supergiant pulsation because the wavelength of internal gravity waves propagating in these extended atmospheres should exceed the cut-off wavelength. The latter results from their radiative damping and the atmospheric curvature. Based on the diagnostic (L, P)-diagram de Jager et al. (1991) pointed out that in the highest atmospheric levels of these stars only the very low-mode (long wavelength) gravity waves are possible. In deeper layers the damping cut-off wavelength becomes gradually shorter and higher gravity waves become possible. The more extended the atmosphere the lower the mode-number of gravity waves that may develop. In very cool stars, like Betelgeuse, for which the atmospheric pressure scale height is an appreciable fraction of the photospheric radius ($\sim 10\%$ of $R_\star$), the convection region is well-developed and can extend up to optical depths as small as 0.3. However, it is known that gravity waves cannot propagate inside convectively stable regions where their minimum period (the Brunt-Väisälä period) becomes real (and non-zero). Gravity waves may arise above the convective layers by penetrative (or overshoot) convective motions. They could be triggered in the very upper photospheric layers and propagate randomly into the lower chromosphere, causing the upflow motions we presently detect.

de Jager & Eriksson (1992) computed that a 440 day pulsation period for Betelgeuse can be interpreted as the period P of photospheric internal gravity waves with a

wavelength L between $R_\star/3$ and $R_\star/30$. These low-order gravity waves propagate nearly horizontally through the photosphere. Non-radial pulsations of the deeper photosphere are a possible source for g-modes that cause similar oscillations of the chromosphere, because the amplitude of the radial velocity curve measured in the optical at Oak Ridge Observatory (Dupree, Lobel, & Gilliland 1999) indicates a redshift by 4 to 5 km s^{-1} during the monitoring period with STIS. An average collapse of the photosphere in the line of sight during this period is consistent with the mean downflow we observe for the larger chromospheric envelope. Localized subsonic upflow in the deeper chromospheric layers can result from photospheric gravity waves that drive the complex chromospheric kinematics, because the total velocity amplitude of ~ 2 km s^{-1} we measure at the inner disk in 1998 September remains within the velocity range of $v = L/P = 0.43$ to 4.3 km s^{-1}, predicted for these waves. But note that this phase-velocity equals the velocity amplitude only for strictly horizontally propagating planar waves. In reality the wavevector of a gravity wave has a radial component as well, and the velocity amplitude will differ from the (group-)velocity of energy propagation.

de Jager & Eriksson (1992) also noted that for Betelgeuse a period of ~ 11 years, reported by Dupree et al. (1990), can result from gravity waves with a wavelength equal to the stellar circumference, or -what is the same- to photospheric non-radial pulsations with $l=1$. It is interesting to note that recent time-dependent 3D hydrodynamic simulations by Jacobs, Porter, & Woodward (1999) of a complete red giant star show highly non-symmetric global dipolar flows within the convective layer, as well as distinct radial pulsations driven by non-linear interactions of acoustic waves with convective motions[3]. Spherical harmonics of the radial velocity are dominated by the dipolar ($l=1$) mode followed, at higher l-values, by a spectrum of modes similar to that of a Kolmogorov turbulence spectrum. They note that the simulated oscillations can be induced by the large-scale convective motions.

A more definitive answer requires detailed hydrodynamic modeling and a stability analysis of our model chromosphere against time-dependent mechanical perturbations. The placement of further constraints on the temporal properties of Betelgeuse's chromospheric dynamics, based on semi-empirical modeling, would greatly benefit from observing near-UV chromospheric emission lines and unblended near-IR absorption lines that form deep in the photosphere, to track the velocity amplitudes and the detailed phase correlation of both atmospheric regions with sufficiently high temporal and spectral resolution, over at least a complete pulsation cycle. Future spectral studies should also comprise spatially resolved high-dispersion observations of the Na I or K I resonance lines to infer the velocity structure of the gas component in the (asymmetric) circumstellar dust shell, to test for possible correlations with the chromospheric kinematics of this supergiant star.

5. CONCLUSIONS

i. Spatially resolved high-resolution spectra of selected emission lines in Betelgeuse's near-UV spectrum reveal self-absorbed optically thick emission lines that display reversals in their component maxima when scanning across the chromospheric disk. We identify four unsaturated emission lines, Si I $\lambda 2516.1$, Fe II $\lambda 2402.6$, Fe II $\lambda 2868.9$, and Al II] $\lambda 2669.2$, that display a very similar evolution of their component maxima and of line morphology during this monitoring period of 15 months. A prominent reversal is observed for these lines in 1998 September at two subsequent scan positions near the disk center.

ii. We model with radiative transport calculations in NLTE and spherical geometry the detailed shape of the Si I $\lambda 2516$ resonance line for different scan positions. The spatially resolved modeling of this component reversal reveals a mean velocity for the chromospheric fluid with opposite flow directions and a difference of velocity amplitude of ~ 2 km s^{-1}. This detailed modeling precludes a strictly radial mean velocity structure for the chromospheric kinematics.

iii. The temporal behavior observed in many other emission lines during this monitoring period indicates a chromospheric oscillation phase with global downflow between 1998 January and 1998 September. For the latter observation date local upflow commenced in deeper chromospheric layers of the Western hemisphere, which extended further towards the Eastern hemisphere in March 1999. This global downflow is consistent with a redshift by 4 to 5 km s^{-1} in the disk-integrated photospheric radial velocity curve observed in the optical.

iv. The detailed modeling of these spatially resolved Si I profiles requires a constant value for macro-broadening of 9 ± 1 km s^{-1} at all scan positions. This implies a strongly isotropic and uniform large-scale velocity field across the stellar chromosphere, but which remains spatially unresolved with the 25 mas by 100 mas field of view. The modeling of the line profiles requires highly supersonic microturbulence velocities in the chromosphere.

v. In general, we observe and measure with elaborate radiative transport calculations an increase of hydrodynamic velocities with a decrease of their length scales in the chromosphere of Betelgeuse. The very large-scale global chromospheric oscillation is non-radial and subsonic. The large-scale macroturbulence is isotropic with a velocity around the isothermal sound speed in the chromosphere. The small-scale microturbulent velocities are subsonic in the stellar photosphere and become highly supersonic in the chromosphere.

---

[3] for images see http://www.lcse.umn.edu/research/RedGiant/

REFERENCES

Airapetian, V. S., Ofman, L., Robinson, R. D., Carpenter, K., & Davila, J. 2000, ApJ, 528, 965

Boesgaard, A. M. 1979, ApJ, 232, 485

Bowen, G. 1988, ApJ, 329, 299

Brandt et al. 1995, AJ, 109, 2706

Byrne, P., Dufton, P., Kingston, A., Lennon, D., & Murphy, H. 1988, A&A, 197, 205

Carpenter, K. G., Pesce, J. E., Stencel, R. E., Brown, A., Johansson, S., & Wing, R. F. 1988, ApJS, 68, 345

Carpenter, K. G., & Robinson, R. D. 1997, ApJ, 479, 970

Carpenter, K. G., Robinson, R. D., Wahlgren, G. M., Linsky, J. L., & Brown, A. 1994, ApJ, 428, 329

Cox, J. P. 1980, Theory of Stellar Pulsation, Princeton University, Princeton, p. 234

Cuntz, M. 1997, ApJ, 325, 709

de Jager, C., de Koter, A., Carpay, J., & Nieuwenhuijzen, H. 1991, A&A, 244, 131

de Jager, C. 1992, in Instabilities in Evolved Super- and Hypergiants, Proceedings of the International Colloquium in Amsterdam, March 1991, ed., C. de Jager and H. Nieuwenhuijzen (Royal Netherlands Academy of Arts and Sciences, Proceedings, Sect. Physics, First Series, Part 36), 98

de Jager, C., & Eriksson, K. 1992, in Instabilities in Evolved Super- and Hypergiants, Proceedings of the International Colloquium in Amsterdam, March 1991, ed., C. de Jager and H. Nieuwenhuijzen (Royal Netherlands Academy of Arts and Sciences, Proceedings, Sect. Physics, First Series, Part 36), 117

de Jager, C., Lobel, A., & Israelian, G. 1997, A&A, 325, 714

de Koter, A., de Jager, C., & Nieuwenhuijzen, H. 1988, A&A, 200, 146

Dupree, A. K., Baliunas, S. L., Guinan, E. F., Hartman, L., Nassiopoulos, G. E., & Sonneborn, G. 1987, ApJ, 317, L85

Dupree, A. K., Baliunas, S. L., Guinan, E. F., Hartmann, L., & Sonneborn, G. 1990, in: Confrontation between Stellar Pulsation and Evolution, eds. C. Cacciari and G. Clementini, ASP Conf. Ser. 11, p. 468

Dupree, A. K., Lobel, A., & Gilliland, R. L. 1999, BAAS, 194, #66.05

ESA 1997, The Hipparcos and Tycho Catalogues (ESA SP-1200)

Fuhr, J. R., Martin, G. A., & Wiese, W. L. 1988, J. Phys. Chem. Ref. Data, Vol 17, Suppl. 4

Freytag, B. 2000, Astronomische Gesellschaft Abstract Series, Vol. 17. Abstracts of Contributed Talks and Posters presented at the Annual Scientific Meeting of the Astronomische Gesellschaft at Bremen, September 18-23, 2000, WWW Electronic Article at: HTTP://WWW.ASTRO.UU.SE/ BF/MOVIE/MOVIE.HTML

Gilliland, R. L., & Dupree, A. K. 1996, ApJ, 463, L29

Goldberg, L. 1984, PASP, 96, 366

Harper, G. 1994, MNRAS, 268, 894

Hartmann, L., & Avrett, E. H. 1984, ApJ, 284, 238

Hayes, D. P. 1981, ApJ, 241, 165

Hayes, D. P. 1981, PASP, 93, 752

Hayes, D. P. 1984, ApJS, 55, 179

Hegmann, M., & Kegel, W. H. 2000, A&A, 359, 405

Honeycutt, R. K., Kephart, J. E., Bernat, A. P., Gow, C. E., Sandford, M. T., II, & Lambert, D. L. 1980 ApJ, 239, 565

Hummer, D. G., & Rybicki, B. G. 1968, ApJ, 153, L107

Jacobs, M. L., Porter, D. H., & Woodward, P. R. 1999, BAAS, 195, #50.04

Judge, P., & Carpenter, K. 1998, ApJ, 494, 828

Kurucz, R. L. 1998, ASOS6, Abstracts of the 6th Atomic Spectroscopy and Oscillator Strengths meeting in Victoria, Aug. 9−13, 1998, Univ. of Victoria, BC, Canada, p. 89

Lobel, A., de Jager, C., Nieuwenhuijzen, H., Smolinski, J., & Gesicki, K. 1994, A&A, 291, 226

Lobel, A., & Dupree, A. K. 2000, ApJ, 545, 454

Mauron, N., 1990, A&A, 227, 141

Mauron, N., & Querci, F. 1990, A&AS, 86, 513

Meaburn, J., López, J. A., & O'Connor, J. 1999, ApJ, 516, L29

Pasquali, A., Nota, A., & Clampin, M. 1999, A&A, 343, 536

Porter, D. H., Woodward, P. R., Anderson, S. E., Winkler K.-H., & Hodson S. W. 1997, Numerical Simulation of Compressible Turbulence, WWW Electronic Article at: HTTP://WWW.LCSE.UMN.EDU/MOVIES/

Querci, M., & Querci, F. 1986, in: Cool Stars, Stellar Systems, and the Sun IV, eds. M. Zeilik and D.M. Gibson, Berlin: Springer, p. 492

Smith, M. S., Patten, B. M., & Goldberg, L. 1989, AJ, 98, 2233

Stencel, R., Linsky, J., Brown, A., Jordan, C., Carpenter, K., Wing, R., & Czyzak, S. 1981, MNRAS, 196, 47P

STScI 1999, *STIS Instrument Handbook*, Version 3.0, Chap. 13

Uitenbroek, H., Dupree, A. K., & Gilliland, R. L. 1998, AJ, 116, 2501

Young, J. S., Baldwin, J. E., Boysen, R. C., Haniff, C. A., Lawson, P. R., Mackay, C. D., Pearson, D., Rogers, J., St.-Jacques, D., Warner, P. J., Wilson, D. M. A., & Wilson, R. W. 2000, MNRAS, 315, 635

FIG. 1.— Four spatially resolved raster scans of Betelgeuse's chromosphere, obtained with STIS between 1998 January and 1999 March. The self-absorbed line profiles of Fe II λ2868.9 (*dash-dotted lines*), Si I λ2516.1 (*solid lines*), and Fe II λ2402.6 (*dotted lines*), observed with medium-resolution and with an aperture size of 25 mas by 100 mas, are shown for three pointing off-sets of 25 mas left and right of intensity peakup (0.0). Note the remarkable reversals in the maxima of the emission line components from scan positions 0.0 to +0.025 in 1998 September. This reversal is modeled for the Si I line in this paper with detailed radiative transport calculations that reveal movements in opposite directions with subsonic mean velocities over the chromospheric line formation region. A high-dispersion observation of the Fe II λ2868.9 line is shown by the dashed lines in the scan of 1998 April. These line profiles are obtained through an aperture of 63 mas by 200 mas for two off-sets of 63 mas, left and right of peakup. The absolute intensity of these profiles has been scaled down for comparison with the medium-resolution scan. The relative intensity of the line components and the line shape do not alter with higher spectral resolution, showing that the medium-resolution observations are useful for the detailed spatially resolved modeling in this paper.
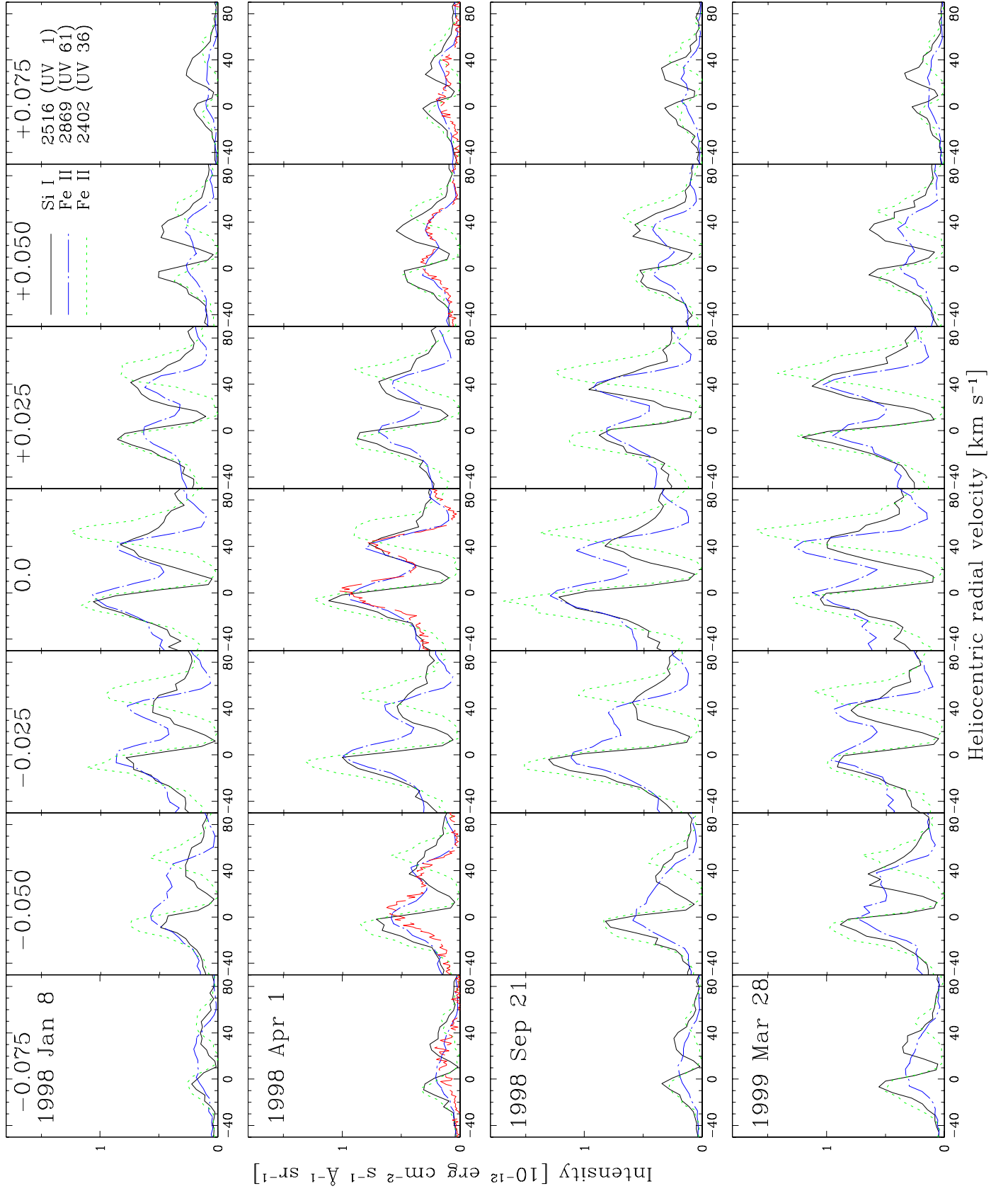
Fɪɢ. 2.— Medium-resolution scans for Al ɪɪ] λ2669.1 (*solid lines*), Fe ɪɪ λ2917.4 (*dotted lines*), Fe ɪɪ λ2880.7 (*long dash-dotted lines*), and Fe ɪɪ λ2984.8 (*short dash-dotted lines*). The Al ɪɪ line also displays the reversal of its component maxima in 1998 September, similar as for the lines in Figure 1 (see text). Line profiles are shown un-smoothed.
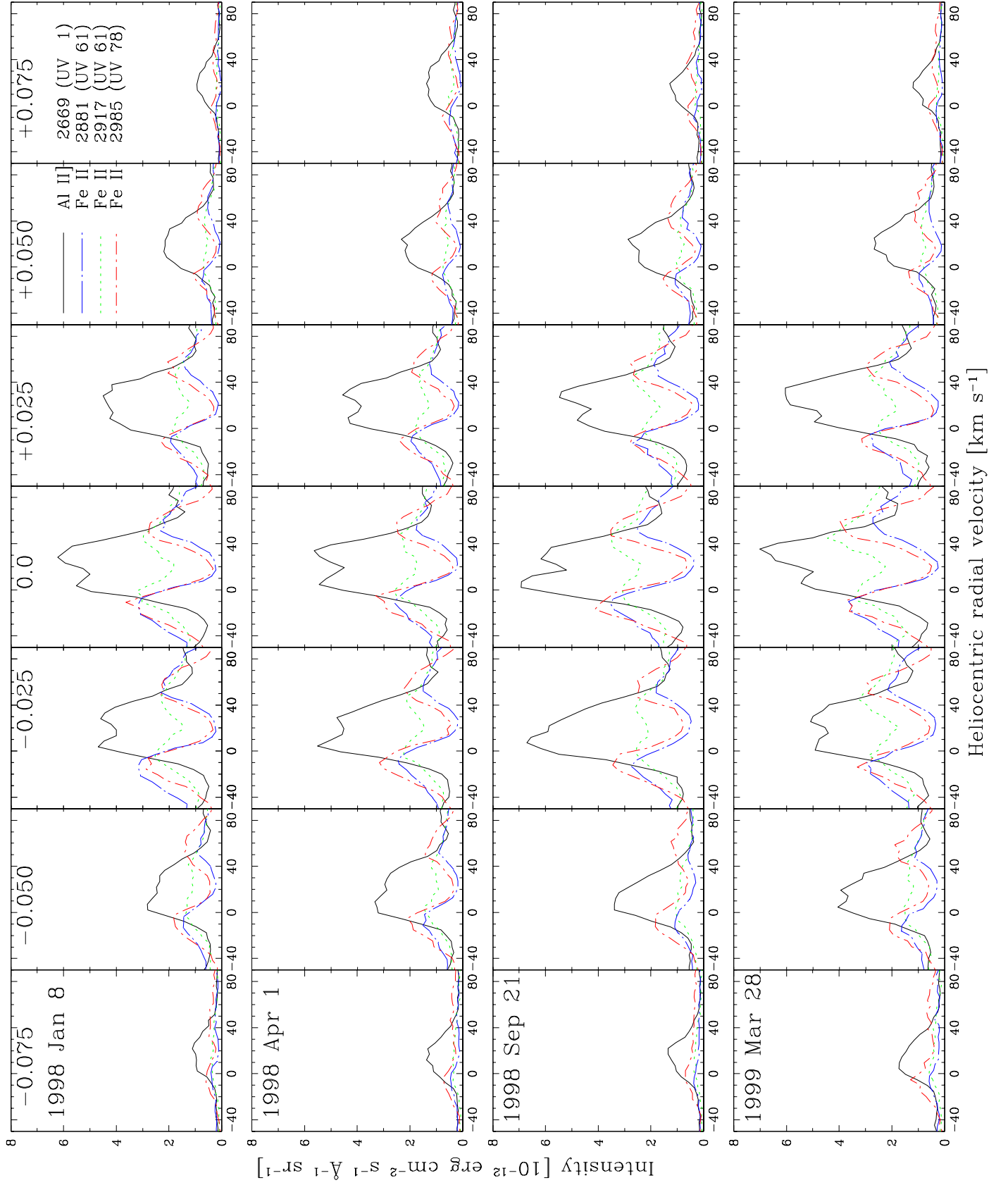
Fig. 3.— Profile changes in unsaturated self-reversed chromospheric emission lines reveal systematic reversals of the emission component maxima near the disk center (TP 0.0, *panels left*; TP +0.025, *panels right*) for the spatial scan of 1998 September 21. The Al II] λ2669 line for these observations is shown for two overlapping echelle orders (*solid lines in upper panels*), which reveals that the instrumental noise remains small. These spatial variations of the component intensities exceed the errorbars provided by the STIS calibration pipeline, shown for the Fe II line (*dash-dotted lines in upper panels*) and the Si I line (*solid lines in lower panels*).
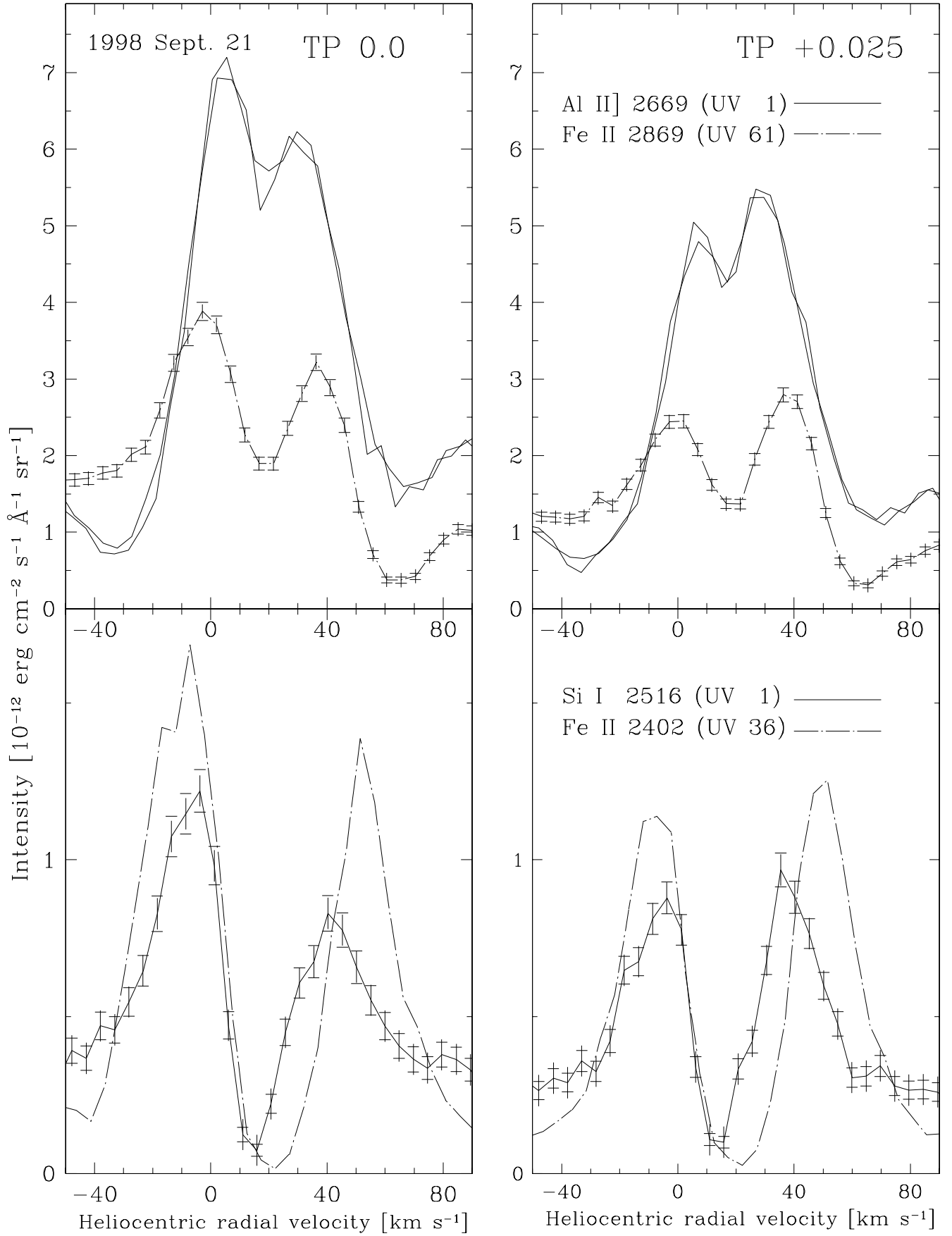
Fig. 4.— *Upper panel:* Portion of Betelgeuse's near-UV spectrum observed with STIS for intensity peakup (TP 0.0) with medium-resolution on 1998 September 21 (*bold solid line*). The LTE synthesis (*thin solid line*) with a hydrostatic model of the chromosphere (Lobel & Dupree 2000) shows that the deep absorption cores result from strong scattering cores of Fe II lines, marked with the vertical lines in the stellar rest frame (top). Note that only Fe I, Fe II, and Cr II lines are shown, although the synthesis also includes other atomic species. A synthesis which includes only iron lines (*dotted line*) already matches this observation very closely. It shows that the UV emission spectrum of the star mainly results from the complex term structure of iron, which causes many blends of very optically thick line transitions in this extended chromosphere. *Lower panels:* An LTE synthesis (static atmosphere) of the Si I λ2516 line shape (*thin dash-dotted line*) matches the observed profile of 1998 September (*bold solid line* for TP 0.0; *dashed solid line* for TP +0.025), after convoluting with the instrumental resolution and macrobroadening of 9 $\mathrm{km\,s^{-1}}$. The two iron lines at the indicated wavelengths are not observed. The profiles computed for the Si I and the Al II line are symmetric, which indicates that their observed spatial component reversals are not influenced by chromospheric blends.
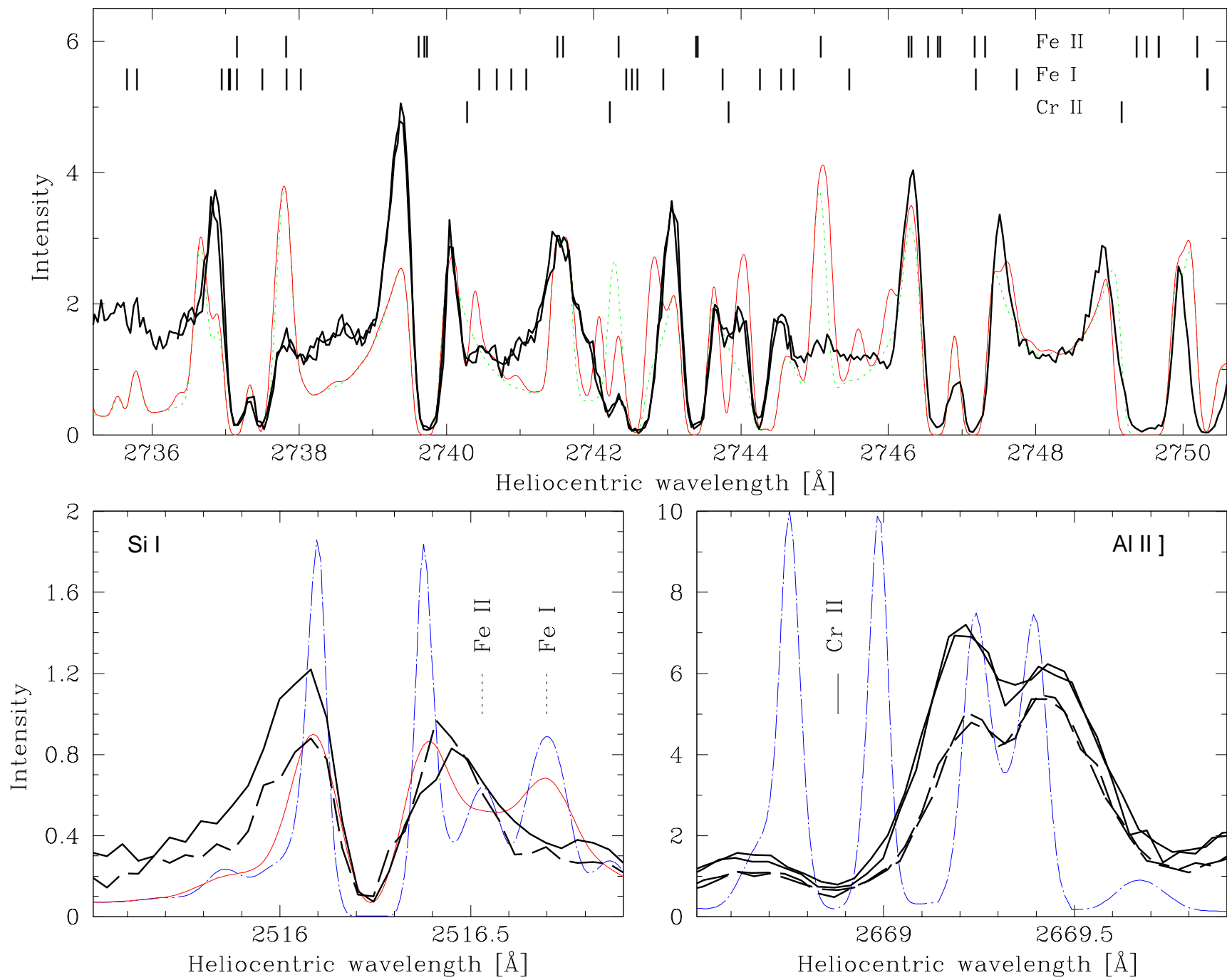
Fig. 5.— Best NLTE fits (*thin solid lines*) to the Si I $\lambda 2516$ line, observed in 1998 September (*bold solid lines*) and in 1998 April (*bold dash-dotted lines*), are computed in spherical geometry with a semi-empirical model of the mean velocity structure in the chromosphere, shown in the upper right-hand panel (*solid line*). This model with downflow reproduces the relative intensity of the emission line components at TP 0.0, but does not fit the intensity reversal observed at TP +0.025 in 1998 September. The component ratios for the positive scan positions are best fit (*thin dash-dotted lines*) with a model of subsonic outflow (*dash-dotted line in upper right-hand panel*). It reveals that the chromosphere assumes a non-radial velocity structure in 1998 September, for which the spatially resolved modeling measures a difference of flow velocity in opposite directions of ~ 2 km s^{-1}. Notice how these spatially resolved calculations also reproduce the reduction in the component ratios, caused by the projection effect, when scanning towards the limb (compare lower panels).
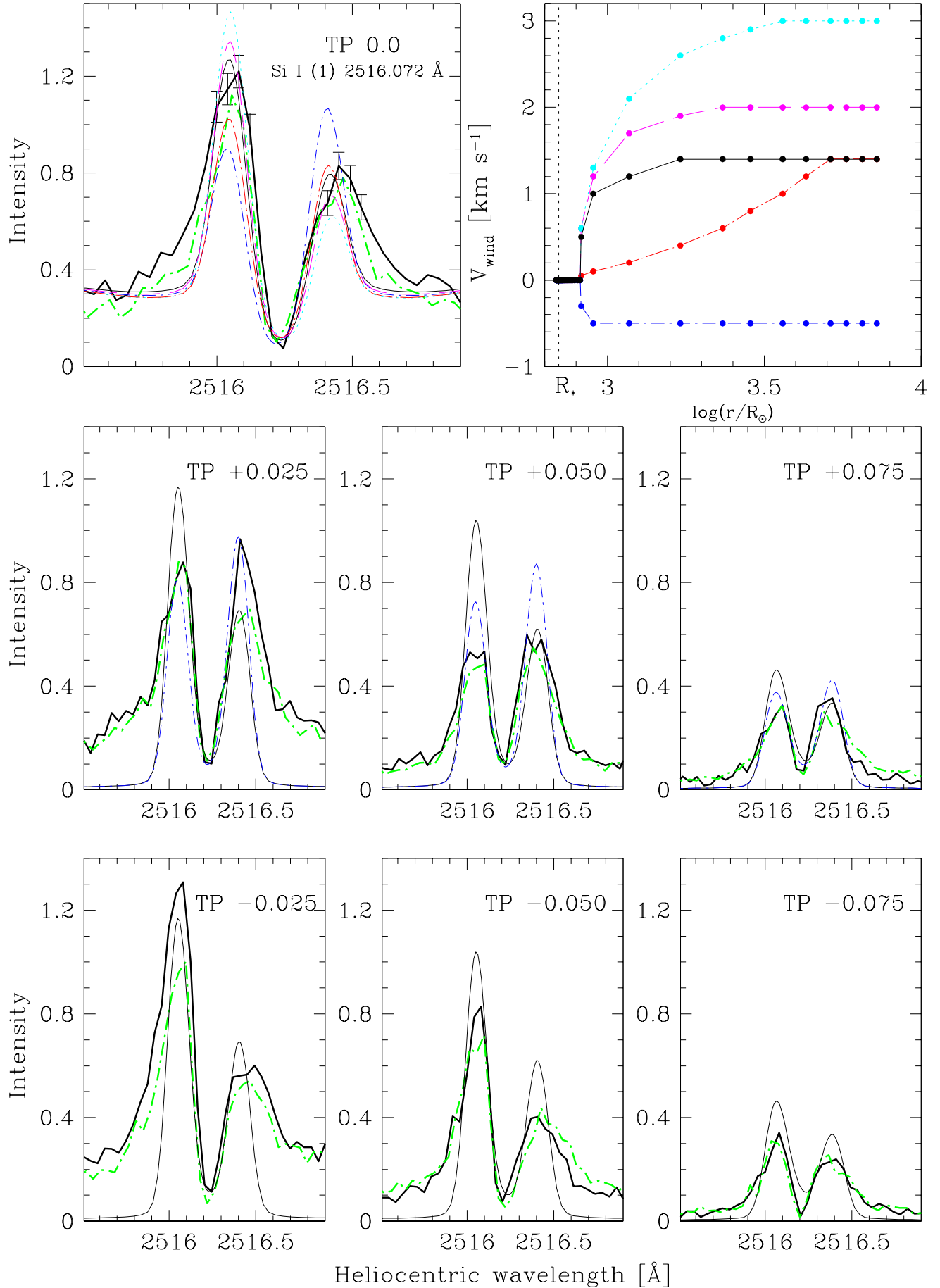
FIG. 6.— Schematic 3D representation of the fluid movements in Betelgeuse's extended chromosphere, based on the spatially resolved semi-empirical modeling of the Si I λ2516 line profile in the STIS raster scans, obtained between 1998 January and 1999 March. Other more optically thick lines define the dynamics at high levels. The global downflow observed for the larger chromospheric envelope in 1998 January and 1998 April, reverses into subsonic upflow in 1998 September for the lower chromospheric layers. It reproduces the reversal in the component maxima of this line, observed for different scan positions of the aperture (*dashed lines*) near the inner chromospheric disk. The photospheric radius is drawn by the dotted circles. The outflow enhances in 1999 March when more symmetric profiles are observed, extending further towards the Eastern (left-hand) front hemisphere. The detailed modeling reveals a local non-radial oscillation of the chromosphere.